International Journal of Heat and Mass Transfer 52 (2009) 1589–1599

Contents lists available at ScienceDirect

International Journal of Heat and Mass Transfer

journal homepage: www.elsevier.com/locate/ijhmt

Numerical investigation and optimization of the thermal performance of a brushless DC motor

Min-Soo Kim, Kwan-Soo Lee *, Sukkee Um

School of Mechanical Engineering, Hanyang University, 17 Haengdang-dong, Seongdong-gu, Seoul 133-791, Republic of Korea

ARTICLE INFO

Article history:
Received 27 November 2007
Received in revised form 16 July 2008
Available online 20 September 2008

Keywords:
Brushless DC motor
Motor cooling system
Motor thermal management
Optimization
Rotating flow

ABSTRACT

A computational study of a brushless DC motor is presented to determine the thermo-flow characteristics in the windings and bearings under the effects of heat generation. The rotation of the rotor blades drives an influx of ambient air into the rotor inlet. The predicted inflow rates were higher at the front inlet than at the rear inlet due to non-uniform pressure distribution. A recirculation zone appeared in the tiny interfaces between windings. The poor cooling performance was caused by flow separation near the groove threshold by the inclination angle of the bearing groove and by a relatively slow velocity near the bearing and between windings. Based on these results, design parameters for the inlet location and geometry, and for the bearing groove geometry, were determined and optimized to enhance the cooling performance up to 24%.

1. Introduction

In a conventional DC motor (brushed DC motor), brushes make mechanical contact with a set of electrical contacts on the rotor, forming an electrical circuit between the DC electrical source and the armature coil windings. Brushless DC (BLDC) motors are widely used because they produce less electrical and mechanical noise, and have a longer durability due to the absence of brushes. However, like conventional DC motors, BLDC motors have many cooling problems because of heat generated by the motor. These problems must be resolved to reduce the overall weight of the motor, and increase its longevity and reliability.

Copper losses due to heat produced by electrical currents in the windings, iron losses from the core, and mechanical losses of the rotating shaft and bearing system all contribute to motor heat generation. These losses have a strong effect on the motor efficiency, rotation speed, and lubrication of the motor bearing, resulting in a thermal aging process and eventually shorting out the motor. Therefore, it is necessary to optimize thermal management and motor cooling systems to increase the longevity and reliability of the motor [1].

The fluid flow in a motor with rotors and stators is a rotating flow problem similar to those for compressors, turbo machines and fans. However, many previous rotating flow studies [2–5] cannot be applied to a motor with heat generation since thermal characteristics were not considered. Imao et al. [2] investigated the effect of the rotational speed of a cylinder on instabilities and turbulence intensity, and Inamuro et al. [3] analyzed flow characteristics according to the speed difference between a cylinder and a disk. Sobolik et al. [4] studied the instabilities of a concentric cylinder with a rotating inner cylinder and stationary outer cylinder for various Taylor numbers, while Hwang and Yang [5] examined the effects of axial flow in a similar concentric cylinder arrangement.

Several studies have examined both fluid flow and thermal characteristics in rotating flow problems. Char and Hsu [6] and Yoo [7] studied the effects of natural convection in concentric cylinders, while Yuan et al. [8] investigated the effect of the Reynolds number and cavity length of a disk cavity. However, these studies could not consider both the axial and tangential flow characteristics because they used two-dimensional (2D) assumptions. Raimundo et al. [9,10] analyzed the effects of a rotating disk in a cylinder using a three-dimensional (3D) simulation, and validated the results with experimental data. These studies only investigated an ideal geometry without obstacles in the cylinder, and were limited to motors with windings that disturb the flow fields. Nakahama et al. [11] analyzed the flow of a BLDC motor for an electric vehicle, and proposed methods such as changing the ribs or altering the interior flow path to decrease the stator winding temperature. However, this study only considered fluid flow, not thermal characteristics, and the design parameters were limited to the ribs and the flow path. Most research concerned with rotating flow problems adopts an ideal cylindrical geometry, making it difficult to apply the results to practical motor applications.

We investigate flow characteristics, taking into account non-ideal geometry (copper windings, insulation, and iron core), and thermal characteristics under the effects of heat generation in a

* Corresponding author. Tel.: +82 2 2220 0426; fax: +82 2 2295 9021.
E-mail address: ksleehy@hanyang.ac.kr (K.-S. Lee).

0017-9310/$ - see front matter © 2008 Elsevier Ltd. All rights reserved.
doi:10.1016/j.ijheatmasstransfer.2008.07.040

Nomenclature

C_2, C_μ	turbulence constants
C_p	specific heat at a constant pressure
d_m	bearing mean diameter (mm)
f_0	factor related to the type of bearing and lubrication method
f_1	factor related to the type of bearing and load
G_k	generation of turbulent kinetic energy
H_f	heat generation of the bearings (W)
H_w	heat generation of the windings (W)
k	thermal conductivity (W/m K)/turbulent kinetic energy (m^2/s^2)
M	total frictional torque (N mm)
M_1	torque due to the applied load (N mm)
M_2	torque due to the viscosity of the lubricant (N mm)
$\dot{m}$	flow rate (kg/s)
n	rotor rotation speed (rpm)/normal direction
Pr_t	turbulent Prandtl number
p	pressure (Pa)
p_1	preload (N)
$\dot{Q}$	heat transfer rate (W)
r, θ, z	radial, axial and azimuthal coordinate
T	temperature (°C)
u	velocity (m/s)
X	design parameter
x	normalized design parameter

Greek symbols

Δ	difference
δ_{ij}	Kronecker delta
ε	turbulent kinetic energy dissipation rate (m^2/s^3)
μ	dynamic viscosity (kg/m s)
ν	kinematic viscosity (m^2/s)
ν_0	kinematic viscosity of bearing lubricant (mm^2/s)
ρ	density (kg/m^3)
σ_k, σ_ε	turbulent Prandtl number of k, ε

Subscripts

b	bearing
eff	effective
f	fluid
ref	reference
s	solid
t	turbulence
wall	wall surface
w	winding

BLDC motor using 3D simulations to evaluate the motor cooling performance. The effects of various design parameters, including the inlet location, geometry, and bearing groove geometry, on the performance of a BLDC motor are analyzed and optimized to improve the motor's performance.

2. BLDC motor geometry and problem formulation

Fig. 1 shows the schematics of an open outer-rotor BLDC motor. The rotating part is composed of permanent magnets, shaft, blades and rotor shell, while the stator includes iron core, windings, electrical insulation and bearing. The rotor shell, which has 20 rotor inlets and blades, acts as a fan which allows external air to flow in and out of the motor system. Permanent magnets are installed inside the rotating part, and the bearings are composed of shafts and ball bearings. Air can flow through the five small bearing grooves.

We know from an electromagnetic analysis that most of the heat in a BLDC motor is generated in the windings [12]. The generated heat must be removed by a combination of conduction and convection. For a high-speed rotating motor, convection heat transfer plays a major role in carrying the generated heat away from the motor, enabling stable motor operation without additional cooling fans, particularly in the open BLDC motor structures considered in this study. Thus, it is of great importance to induce airflow through the rotor inlets to effectively control the inside temperature of the motor. Internal recirculation or flow separation around the winding surfaces can cause a buildup in local temperatures. Therefore, a careful design strategy is required to enhance the flow influx, minimize the flow separation, and suppress internal recirculation, to ensure the performance and reliability of a BLDC motor.

2.1. Governing equations and boundary conditions

The present model assumes that

(1) the working fluid is air and its properties remain constant;
(2) the flow is 3D, steady-state, incompressible, and turbulent;
(3) the thermal contact resistance is negligible at the solid–solid interfaces.

Taking the rotational speed (n = 1200 rpm) as references, Taylor number [4] of the rotating flow problem is 254. Since the flow is highly turbulent, a renormalized group (RNG) k–ε model was chosen for the flow analysis. Using the above assumptions, the following governing equations were used for the continuity, momentum, turbulent kinetic energy, turbulent kinetic energy dissipation, and energy conservation principles.

2.1.1. Fluid region

Continuity:

$$\frac{\partial}{\partial x_i}(\rho u_i) = 0 \tag{1}$$

Momentum:

$$\frac{\partial}{\partial x_j}(\rho u_i u_j) = -\frac{\partial p}{\partial x_i} + \frac{\partial}{\partial x_j}\left[(\mu + \mu_t)\frac{\partial u_i}{\partial x_j}\right] \tag{2}$$

Turbulent kinetic energy:

$$\frac{\partial}{\partial x_j}(\rho u_j k) = \frac{\partial}{\partial x_j}\left[\left(\mu + \frac{\mu_t}{\sigma_k}\right)\frac{\partial k}{\partial x_j}\right] + G_k - \rho\varepsilon \tag{3}$$

Turbulent kinetic energy dissipation:

$$\frac{\partial}{\partial x_j}(\rho u_j \varepsilon) = \frac{\partial}{\partial x_j}\left[\left(\mu + \frac{\mu_t}{\sigma_\varepsilon}\right)\frac{\partial \varepsilon}{\partial x_j}\right] - C_2\rho\frac{\varepsilon^2}{k + \sqrt{\upsilon\varepsilon}} \tag{4}$$

Energy:

$$\rho C_p \frac{\partial}{\partial x_j}(u_j T) = k_{eff}\frac{\partial^2 T}{\partial x_j^2} + (\tau_{ij})_{eff}\frac{\partial u_i}{\partial x_j} \tag{5}$$

where

$$\mu_t = \rho C_\mu \frac{k^2}{\varepsilon} \tag{6}$$

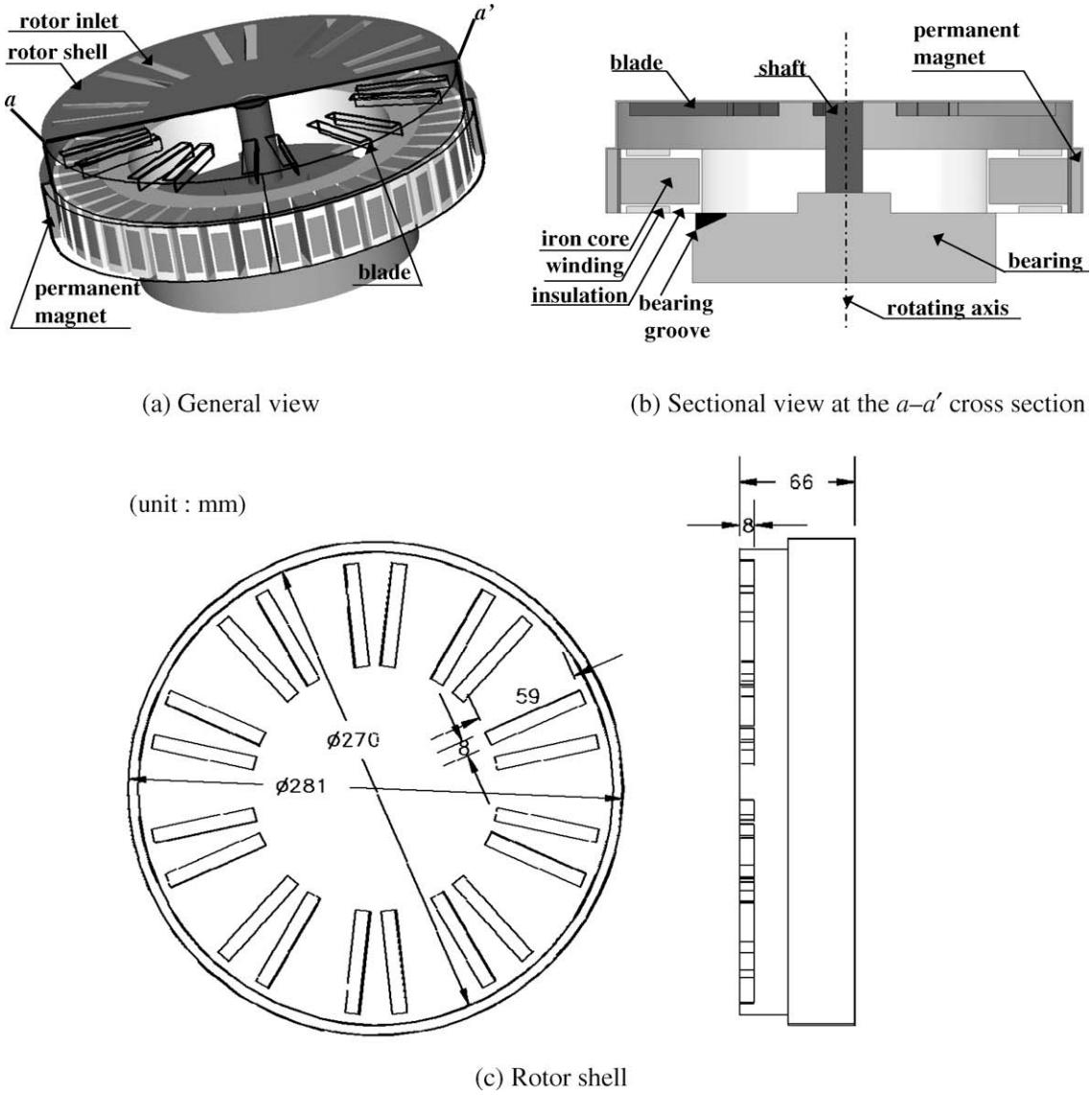

Fig. 1. Schematic diagram of the BLDC motor.

$$G_k = 2\mu_t S_{ij} S_{ij} = \mu_t \left(\frac{\partial u_j}{\partial x_i} + \frac{\partial u_i}{\partial x_j} \right) \frac{\partial u_i}{\partial x_j} \tag{7}$$

$$C_2 = 1.92, \quad C_\mu = 0.09, \quad \sigma_k = 1.0, \quad \sigma_\varepsilon = 1.3 \tag{8}$$

$$(\tau_{ij})_{\text{eff}} = \mu_{\text{eff}} \left(\frac{\partial u_j}{\partial x_i} + \frac{\partial u_i}{\partial x_j} \right) - \frac{2}{3} \mu_{\text{eff}} \frac{\partial u_i}{\partial x_i} \delta_{ij}, \qquad k_{\text{eff}} = k_f + \frac{C_p \mu_t}{\text{Pr}_t}, \quad \mu_{\text{eff}} = \mu + \frac{\mu_t}{0.9} \tag{9}$$

2.1.2. Solid regions

The material properties for the solid iron core, insulation, windings, rotor shell, shaft, and ball bearings are listed in Table 1. The following conduction equation was applied to account for the internal heat transfer:

$$k_{s,j} \frac{\partial^2 T}{\partial x_j^2} + S_g = 0 \begin{cases} S_g = H_w / \rho V_w \\ S_g = H_f / \rho V_b \\ S_g = 0 \text{ in other case} \end{cases} \tag{10}$$

where V_w and V_b are volume of winding and bearing, respectively.

Table 1
Physical properties of the motor components

Components	Density, ρ (kg/m^3)	Thermal conductivity, k (W/m K)	Specific heat, C_p (J/kg K)
Iron core (electrical steel)	7800	25/1.97 (radial/axial)	460.54
Insulation (polybutylene terephthalate, 30% glass fiber filled)	1500	0.25	2300
Magnet (ferrite magnet)	4950	1.257	735
Winding (copper)	8978	387.6	381
Rotor shell (electrical steel)	7800	25	460.54
Bearing (electrical steel)	7800	25	460.54

2.1.3. Interfacial boundary conditions

At the interface between the fluid and solid, the boundary conditions were chosen as

$$\begin{aligned} &\upsilon_r = \upsilon_\theta = \upsilon_z = 0 \text{ at non-rotating wall} \\ &\upsilon_r = \upsilon_z = 0, \ \ \upsilon_\theta = \Omega r \text{ at upper rotor shell} \\ &\upsilon_r = \upsilon_z = 0, \ \ \upsilon_\theta = \Omega R_s \text{ at rotor shell side wall} \end{aligned} \tag{11}$$

$$T_{f,wall} = T_{s,wall}, \quad k_f \frac{\partial T_f}{\partial n}\bigg|_{wall} = k_s \frac{\partial T_s}{\partial n}\bigg|_{wall} \tag{12}$$

where R_s is radius of rotor shell.

2.1.4. Symmetric boundary conditions

Due to symmetry, only one-fifth of the motor geometry was computed. Periodic boundary conditions [12,13] were used for the fluid, while a symmetrical boundary condition was used for the solid:

$$\frac{\partial T_s}{\partial n}\bigg|_{\text{sectional wall}} = 0 \tag{13}$$

2.1.5. Windings and bearings

For the windings, the phase coil current (I), phase coil resistance (R), and coil resistivity were 2.03 A, 4.1 Ω, and 2.141×10^{-8} Ω m, respectively. There were 12 slots for each phase. The amount of heat generated by the windings was determined using

$$H_w = I^2 R/12 \tag{14}$$

For the bearings, the correlation used to estimate the heat generation [14] was expressed as

$$H_f = 1.047 \times 10^{-4} \text{ nM} \tag{15}$$

$$M = M_1 + M_2 \tag{16}$$

where

$$M_1 = f_1 p_1 d_m \tag{17}$$

$$M_2 = \begin{cases} 160 \times 10^{-7} f_0 d_m^3, & v_0 n \leqslant 2000 \\ 10^{-7} f_0 (v_0 n)^{2/3} d_m^3, & v_0 n \geqslant 2000 \end{cases} \tag{18}$$

In this study, only the heat that was generated by the torque related to the applied load (M_1) was considered, since the heat generated by the lubricant friction (M_2) was assumed to be negligible. Also, we neglect the iron loss because iron loss is less than the winding loss [12].

2.2. Numerical procedure

Due to symmetry, only one-fifth of the entire computational domain (θ = 0–72°) was modeled, as shown in Fig. 2. Fig. 2(a) is entire numerical domain which includes the motor and outside space limited by an acrylic case without openings. Detailed grid structure is showed in Fig. 2(b) and (c). A staggered mesh with non-uniform grid spacing is used. The SIMPLE algorithm was used to solve the pressure and flow fields. A second-order upwind scheme was used to discretize the governing equations, particularly the convective terms in each conservation equation, to obtain a more accurate numerical solution. Stringent numerical tests were performed to

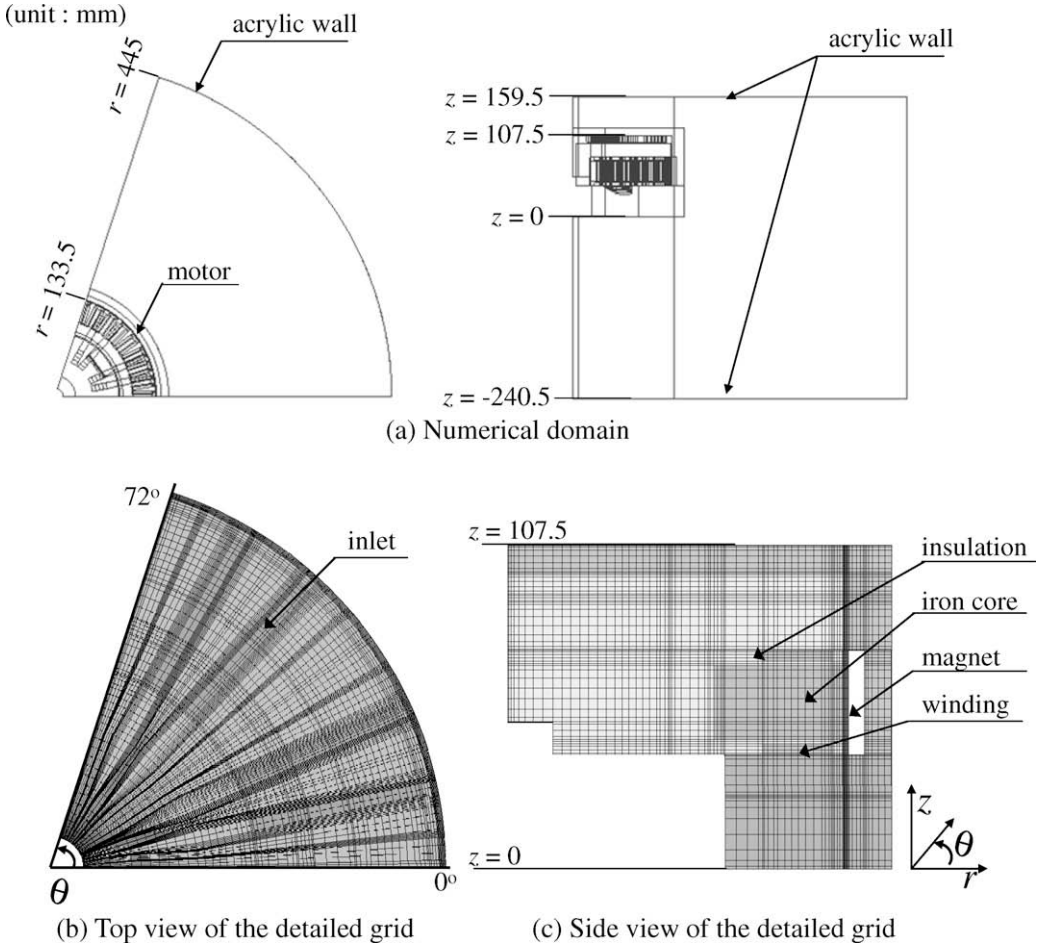

Fig. 2. Schematic configuration and grid generation for the numerical analysis.

ensure that the solutions were independent of grid size. A mesh with 1,191,492 grid points provided sufficient spatial resolution. A highly dense grid was assigned to the narrow viscous sublayer region near the wall boundaries to more precisely capture the turbulent effects. The coupled equations were solved simultaneously, and the solution was deemed to converge when the relative error of each field between two consecutive iterations was less than 10^{-5}.

3. Results and discussion

To validate the numerical model, comparisons were made to our own experimental data, which were collected at the six data points depicted in Fig. 3. The experimental setup consisted of an acrylic case, a motor, a motor driver, a current probe, an oscilloscope, a data acquisition system (National Instruments, SCXI-1600, USB DAQ System) and a thermocouple (Omega, Kapton insulated thermocouple wire, K-type, 24 gauge). Results were also compared using several turbulence models, i.e. including the RNG k–ε [13], the standard k–ε [15], and the realizable k–ε model [16]. As shown in Table 2, the RNG k–ε turbulent model gave results that were closest to the measured data.

In the following numerical analysis, the flow and temperature fields in the BLDC motor were investigated to gain fundamental insight into the motor flow. Then the major cooling issues were addressed by incorporating the RNG k–ε model, followed by in-depth parameter studies. The location and shape of the rotor inlet were varied to induce more flow into the motor system, and additional numerical simulations were performed as a function of the angle of the bearing groove in an effort to lower the temperature near the bearing.

3.1. Thermo-flow analysis in the BLDC motor

To investigate the motor cooling performance, we first considered the overall flow and temperature fields in the motor. Fig. 4 shows the velocity vectors and temperature field at section a–a′ ($\theta = 36°$). The fluid entering through the rotor inlet was centrifuged toward the rotor shell sidewall and deflected downward so that it removed the heat from the windings, and then exited the motor. The inflow through the bearing groove due to the back pressure in the inner motor cooled the space that was heated due to M_1, and then moved upward. Flow near the rotor rotated rapidly because of the high rotation speed (1200 rpm), so the temperature of the winding near the rotor shell was less than that near the bearing. The cooling performance of the bearing was poor because the temperature of the inflow through the bearing groove was high. This was caused by the groove's proximity to the windings. The flow was separated at the heat generation surface. The flow velocity near the bearing was less than that near the rotor shell due to inefficient rotation. Therefore, the bearing temperature was higher than the winding temperature. Moving upward along the bearing surface, the temperature decreased sharply because the heat generated by the bearing was relatively small compared with heat generated by the winding.

The rotor shell consisted of four rotor inlets (for a total of 20), as shown in Fig. 5(a). Two inlets formed a pair. The blade was located to the left of the inlet when viewed from the top. The left and right inlets of each pair were denoted as the front and rear inlets, respectively. The angle between the front and rear inlets of each pair (α) was 12°, while the angle between the rear and front inlets of the adjacent pair (β) was 24°. Fig. 5(b) and (c) shows the flow field at the central section of each inlet. The flow in the upper rotor shell was centrifuged away, along the upper rotor shell, and moved downward along the inner side of the outer rotor shell through the rotor inlets. This caused large pressure variations near the inlet, and large pressure gradients along the far-inner and far-outer sides

Table 2
Comparison of temperature with experimental data

Model	Measured point	Temperature (°C)	Relative error (%)
Experiment	1	33.4	–
	2	33.9	–
	3	34.5	–
	4	37.9	–
	5	38.0	–
	6	37.9	–
Standard k–ε turbulence model	1	35.420	6.05
	2	35.404	4.44
	3	35.385	2.57
	4	38.950	2.77
	5	37.037	2.53
	6	38.950	2.77
RNG k–ε turbulence model	1	35.038	4.90
	2	35.043	3.37
	3	35.043	1.57
	4	37.999	0.26
	5	36.780	3.21
	6	37.999	0.26
Realizable k–ε turbulence model	1	34.589	3.56
	2	34.611	2.10
	3	34.625	0.36
	4	37.084	2.15
	5	34.914	8.12
	6	37.084	2.15

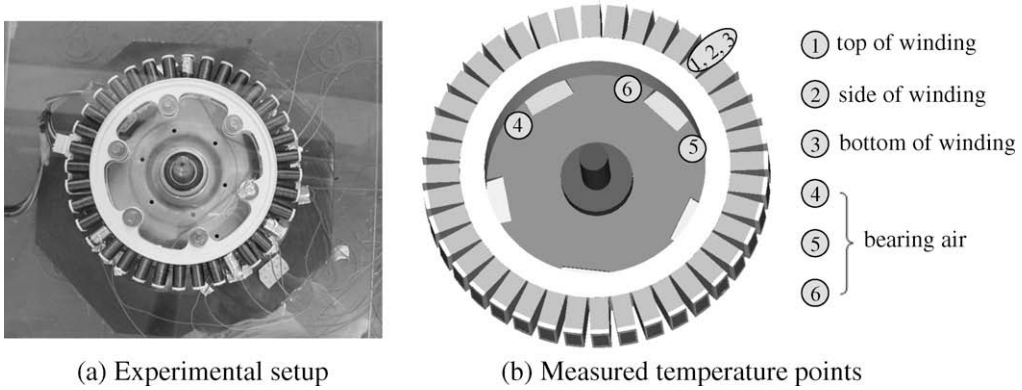

Fig. 3. Measured data points of the motor in the experiment.

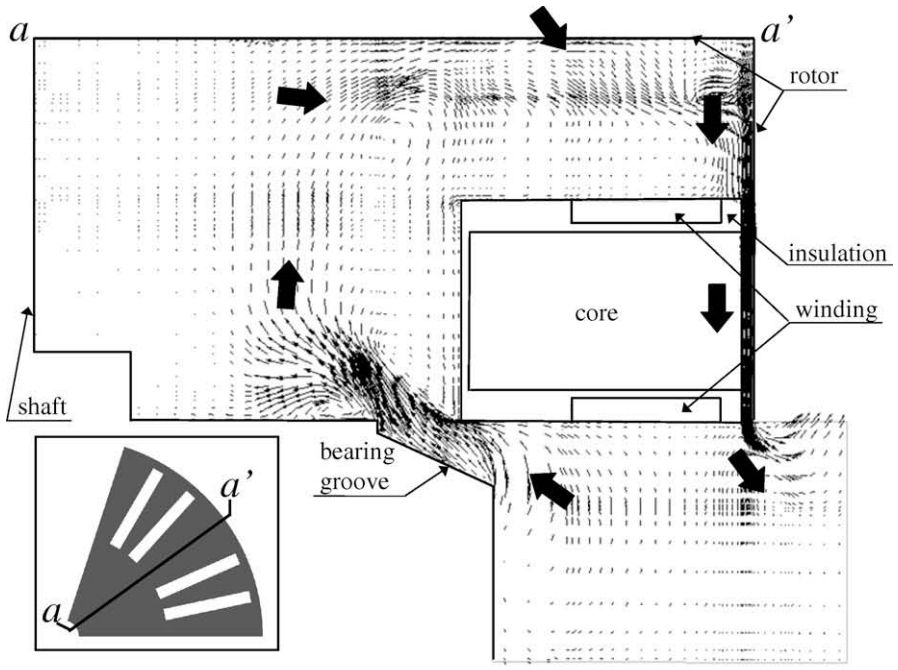

(a) Velocity vectors

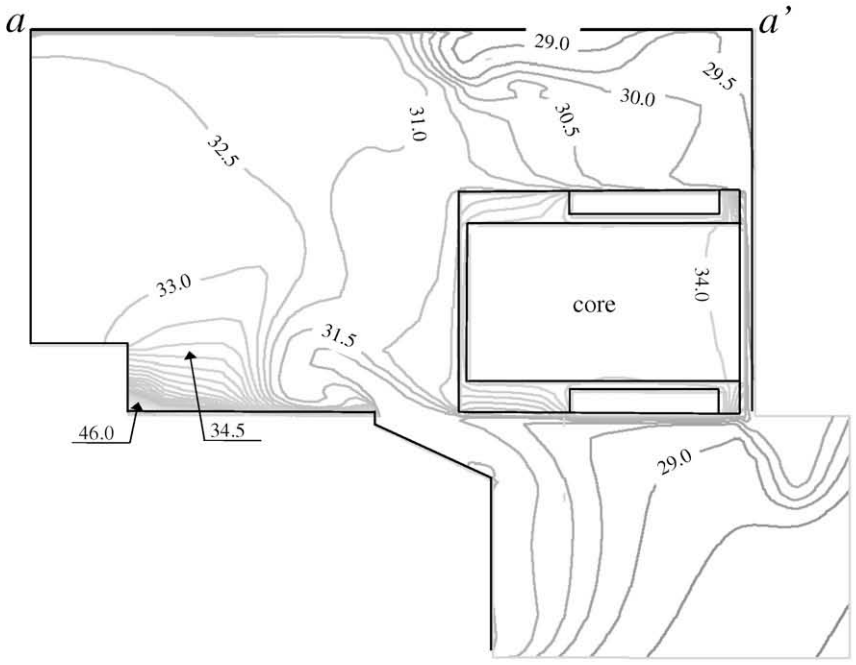

(b) Temperature contours, °C

Fig. 4. Velocity vectors and temperature contours at the a–a' cross-section (at $\theta = 36°$).

of the inlet in the radial direction. Most of the flow entered through the far-inner side of the inlet due to the lower pressure in the lower rotor shell space, denoted in the figure as "L". Fluid coming through the rotor inlet was centrifuged toward the rotor shell sidewall, and most of it was driven into the corner. This increased the pressure at the corner of the rotor shell sidewall, inducing an efflux of external air at the far-outer side of the inlet in the radial direction. Therefore, the rotor inlet should be located in the inner regions. The inner length of the rotor inlet (closest to the center) should be increased, while the outer length of the rotor inlet (farthest from the center) should be shortened to increase the incoming flow rate.

The windings generate heat due to copper losses. To remove this heat effectively, it is necessary to obtain the maximum flow velocity and the minimum flow separation near the heated surface. Fig. 6 shows the winding, including the air gap between the magnet and the winding, and the air gap between windings. The fluid between the magnet and winding rotated rapidly with the magnet, as shown in Fig. 6(a). This fluid collided with the insulation between the wind-

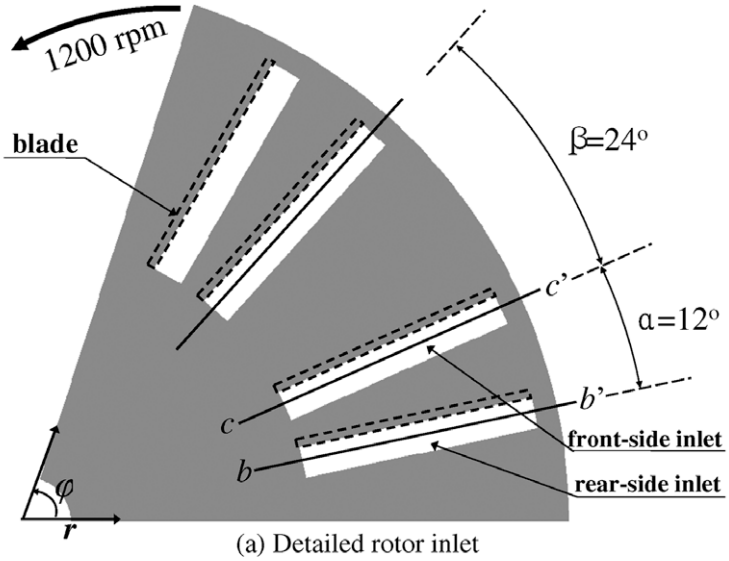

(a) Detailed rotor inlet

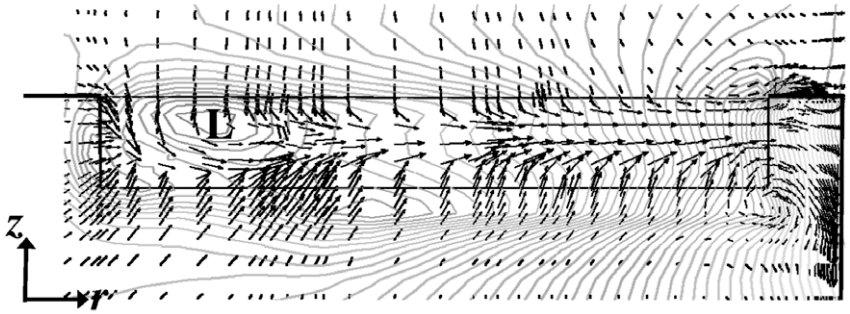

(b) b–b' cross section

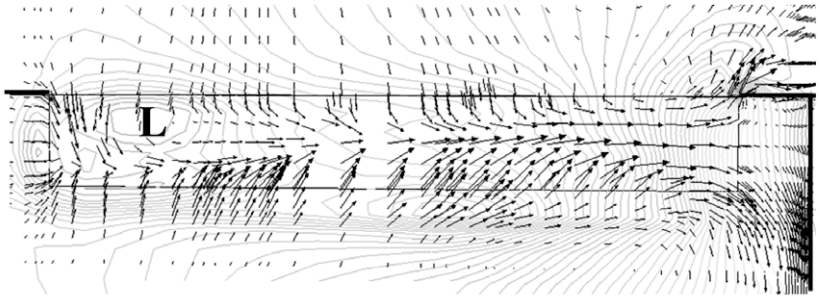

(c) c–c' cross section

Fig. 5. Pressure contours and velocity vectors around the rotor inlet.

ings, creating a high-pressure region. However, the predicted pressure on the opposite side was low, inducing flow recirculation. Therefore, a high-temperature field appeared at the inner side of the windings in the radial direction since the flow velocity was low. This caused a clockwise recirculation because the flow was instable in the upper region, as shown in Fig. 6(b). Thus, the local temperature became higher in the upper region than the lower region, as shown in Fig. 6(c). In this study, we intended to induce fluid flow directly into the windings, and minimize the flow separation to improve the cooling performance. However, we cannot manipulate the winding geometry because it is difficult in practice to alter the shape of windings. Thus, the cooling performance of the windings must be improved by changing other design parameters, such as the inlet location or geometry.

The bearing generated a relatively small amount of heat compared to the winding. However, the local temperature of the bearing was higher than that of the winding as shown in Fig. 4 because the incoming fluid through the groove separated from the bearing surface rather than flowing along it. The separation was caused by the bearing groove which had an inclined angle with a threshold, as shown in Fig. 7. Fluid flowed along the inclined groove and separated around the threshold. The amount of flow was relatively small, producing a local recirculation near the bearing surface. As a result, the incoming flow was not sufficient to cool down the entire heated bearing surface. The bearing is located near the axial shaft and has a relatively small centrifugal effect on the fluid motion. Thus, to increase the cooling performance at the bearing, it is necessary to decrease the flow separation near the surface, induce

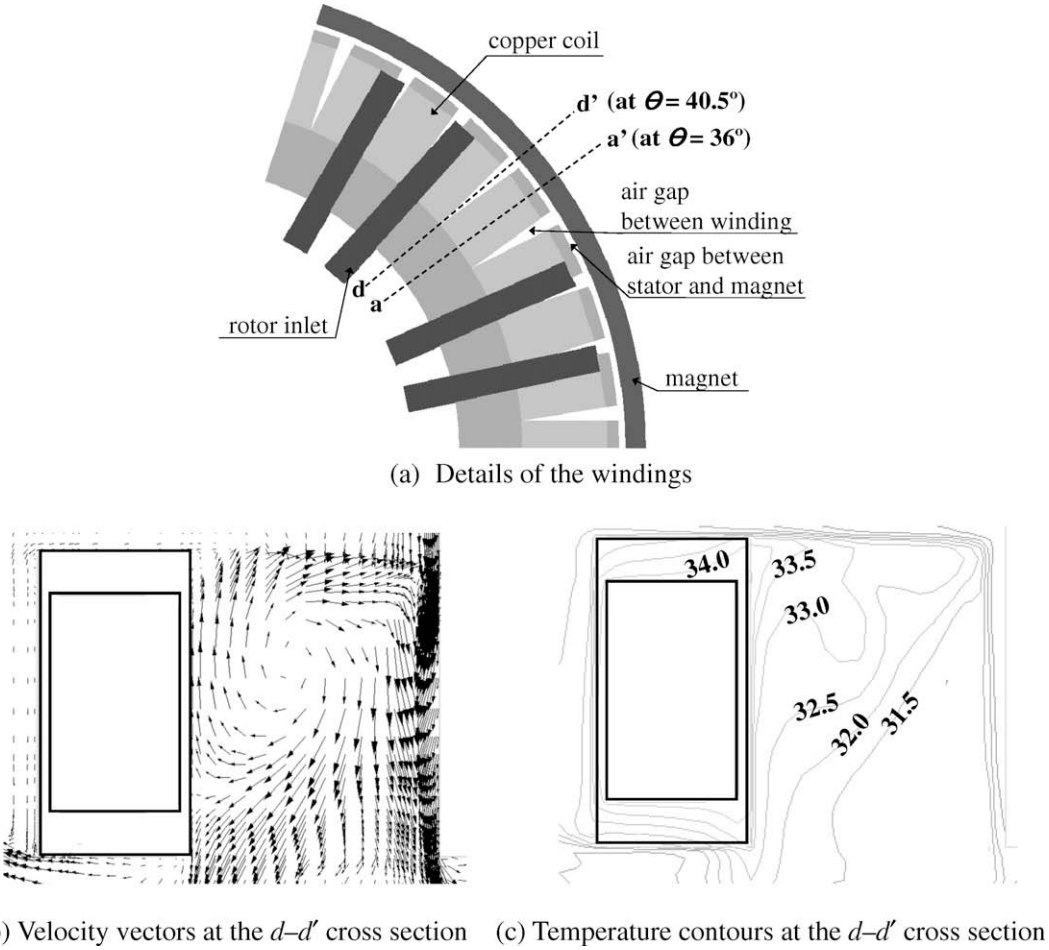

Fig. 6. Flow field and temperature contours around the winding.

the flow to the surface using the groove inclination angle, and improve the rotating effect.

3.2. Effects of the design parameters

In the previous sections, we investigated the general flow and temperature fields in a BLDC motor. According to the thermo-flow analysis, the rotor inlet location should be shifted inward in the radial direction, and the rotor inlet and bearing groove geometries should be modified as shown in Fig. 7 to obtain an optimal design. In this section, we explore the effect of these variations on the cooling performance of the motor.

The rotor inlet location (X_1) was moved inward in the radial direction to increase the incoming flow rate. Values of X_1 = 129 mm to X_1 = 109 mm were considered. At first, the total incoming flow rate increased as the inlet location was moved inward, as shown in Fig. 8(a). However, the total incoming flow rate decreased when X_1 < 119 mm because the centrifugal effect from the rotor blade decreased. A radial location of X_1 = 119 mm improved the flow rate by 33% compared to the reference location at X_1 = 129 mm. As the radial location was moved inward, the heat transfer rate increased proportionally due to the increased flow rate, reaching a maximum at X_1 = 114 mm. The heat transfer rate, that incoming air gets from the motor, was enhanced by 17% and 22% at X_1 = 119 and 114 mm, compared with the reference value. The heat transfer rate was higher at X_1 = 114 mm because more flow was induced into windings, even though the total flow rate was less. Fig. 8(b) shows that the additional direct flow into the winding squeezed the vortex in the air gap between the windings, improving the cooling performance. The additional direct flow into the winding was more important than the actual flow rate when considering the cooling performance.

The inner length (X_2) of the rotor inlet was increased while the outer length (a) of the rotor inlet was decreased to increase the incoming flow rate. For the same inlet area, the sum of the inner and outer lengths was fixed at 16 mm. For example, when the inner length was 12 mm, the outer length was 4 mm. The inner length was varied between 8 and 12 mm. Fig. 9 shows that the total incoming flow rate increased with the inner length because the influx increased and the efflux decreased. A length of X_2 = 12 mm increased the flow rate by 16% as compared with the reference length, X_2 = 8 mm. However, the heat transfer rate increase was only slight, approximately 3.7%, because varying the inlet geometry did not direct more flow onto the windings.

We also examined the bearing design parameters, such as the threshold angle (X_3), the inclination angle (X_4), and the biased angle (X_5), to improve the cooling performance of the bearing surface. Table 3 shows the predicted heat transfer coefficients as functions of the bearing design parameters. The threshold angle was varied between 0° and 65°. When the threshold angle equaled the inclination angle ($90° - X_3 = X_4$), that is, at a threshold angle of 65°, the heat transfer coefficient of the bearing surface improved by 5.5% due to the decrease in flow separation. To induce fluid onto the bearing surface, the inclination angle (X_4) was varied between

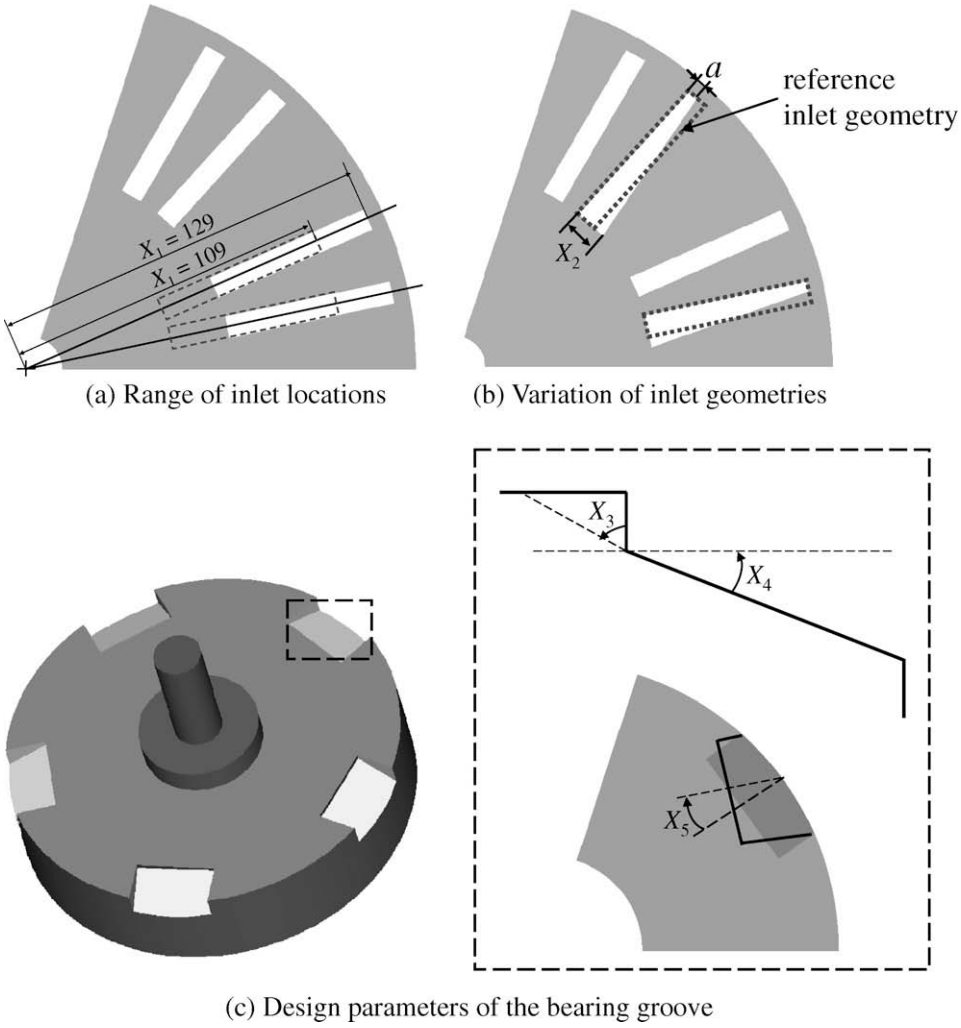

(a) Range of inlet locations (b) Variation of inlet geometries

(c) Design parameters of the bearing groove

Fig. 7. Design parameters of the BLDC motor.

25° and 0°. An inclination angle with a greater slope led to more fluid at the surface, but the incoming flow rate through the groove decreased since the groove inlet decreased. To make use of the rotation effects, we also varied the biased angle between 0° and 15°. However, no improvement occurred in the cooling because we could not eliminate the flow separation. Therefore, only the threshold angle influenced the cooling performance of the BLDC motor when considering variations in the bearing groove geometry.

4. Optimization

We selected the inlet location (X_1), inlet geometry (X_2), and groove threshold angle (X_3) as the design variables to be optimized. These variables were normalized as shown in Table 4. The following optimum design problem was defined, considering an objective function and constraint conditions, and using normalized design parameters (x_1,x_2,x_3):

$$\begin{aligned} &\text{Find } x_1, x_2, x_3 \\ &\text{to maximize } \dot{Q}(x_1, x_2, x_3) \\ &\text{subject to } -1 \leqslant x_1, x_2, x_3 \leqslant +1 \end{aligned} \tag{19}$$

A second-order polynomial was used to estimate the full quadratic model for the response surface. Fifteen experimental points for the optimization, shown in Table 5, were selected using a central composite design to create a response surface. Based on the experimental points, the following response surface was generated using the objective function and constraint conditions:

$$\begin{aligned} \dot{Q}(x_1, x_2, x_3) = {} & 53.0302 - 3.8124x_1 + 0.2274x_2 - 0.4167x_3 \\ & - 3.04122x_1^2 + 0.521778x_2^2 - 0.231722x_3^2 \\ & + 0.514875x_1x_2 + 0.153125x_1x_3 \\ & + 0.035375x_2x_3 \end{aligned} \tag{20}$$

An analysis of variance (ANOVA) was performed to validate the accuracy of the response surface, yielding a coefficient of determination (R^2) of 0.994. Based on Eq. (20), the optimal point was determined as

$$x_1 = -0.5, \quad x_2 = 0.0, \quad x_3 = 1.0 \tag{21}$$

These results indicate that the optimal inlet location, geometry, and groove threshold angle were 114 mm, 65 mm, and 65°, respectively. At this design point, the performance of the optimum model was 24.3% better than the reference model.

5. Conclusions

We conducted a numerical investigation of the cooling performance of a BLDC motor. After analyzing the thermo-flow charac-

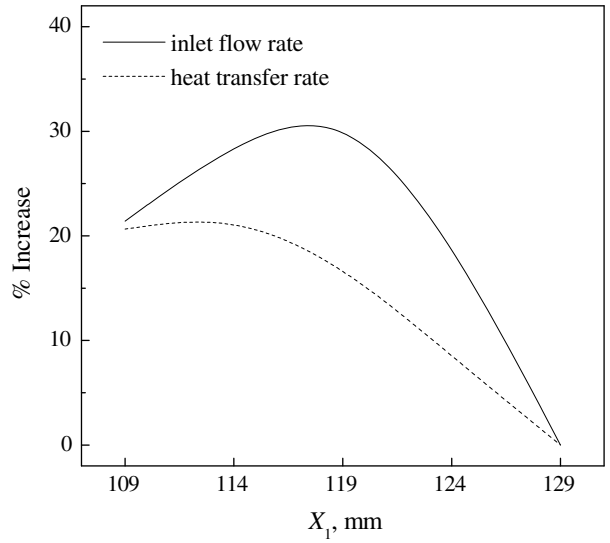

(a) Increase of the inlet flow rate and heat transfer rate as functions of the inlet location

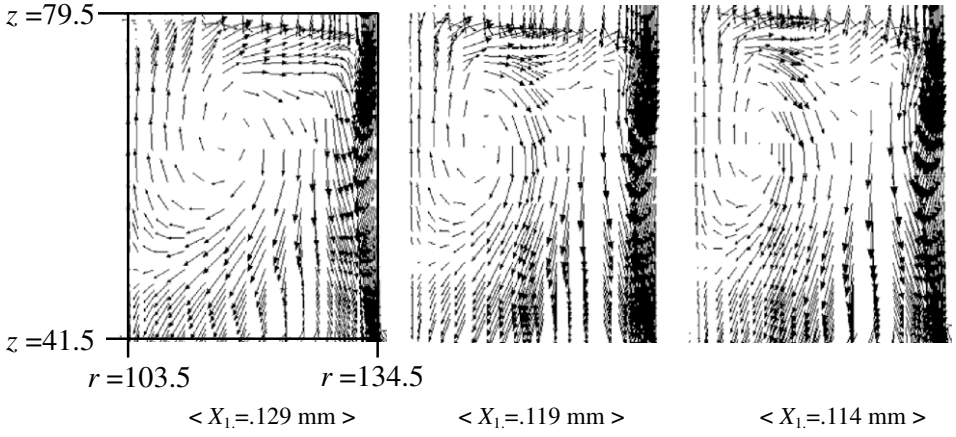

(b)Velocity vectors in the air gap between windings

Fig. 8. Motor performance as a function of the inlet location and geometry.

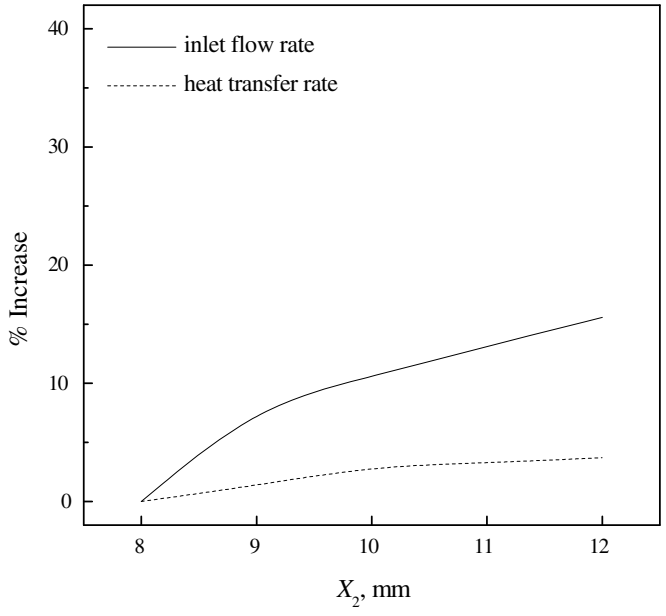

Fig. 9. Increase of the inlet flow rate and heat transfer rate as functions of the inlet geometry.

Table 3
Heat transfer coefficient as a function of the bearing design parameters

Design parameters	Average temperature at the bearing surface (°C)	Average heat transfer coefficient (W/m^2 K)	Rate of increase (%)
Groove threshold angle (X_3, °)			
0[a]	44.40	39.57	–
16.25	44.23	39.68	0.28
32.5	44.07	39.82	0.63
48.75	43.46	41.00	3.61
65	43.35	41.74	5.48
Groove incline angle (X_4, °)			
25[a]	44.40	39.57	–
18.75	44.12	41.10	3.87
12.5	44.56	40.18	1.54
6.25	44.55	39.79	0.55
0	44.41	38.56	−2.55
Groove biased angle (X_5, °)			
0[a]	44.40	39.57	–
3.75	44.37	39.65	0.20
7.5	44.34	39.77	0.51
11.25	44.15	40.02	1.14
15	44.09	40.21	1.62

[a] Reference model.

Table 4
Range of the normalized design parameters

Design parameter	Normalization		
	−1 (lower)	0	+1 (upper)
Inlet location (X_1) (mm)	109	119	129
Inlet geometry (X_2) (mm)	8	10	12
Threshold angle (X_3) (°)	0	32.5	65

Table 5
Design of experiments

Test number	Normalization units			$\dot{Q}$ (W)
	x_1	x_2	x_3	
1	−1	−1	−1	55.221
2[a]	1	−1	−1	45.769
3	−1	1	−1	54.419
4	1	1	−1	47.462
5	−1	−1	1	53.720
6	1	−1	1	45.316
7	−1	1	1	53.495
8	1	1	1	46.715
9	−1	0	0	53.312
10	1	0	0	46.781
11	0	−1	0	53.505
12	0	1	0	53.714
13	0	0	−1	53.127
14	0	0	1	52.585
15	0	0	0	52.800

[a] Reference model.

teristics, the cooling performance was evaluated using various rotor inlet locations and geometries, and bearing groove geometries. These were optimized to achieve the best cooling performance.

The fluid entering the motor through the rotor inlet was centrifuged toward the rotor shell sidewall and deflected downward, removing the heat from the windings. The fluid then exited the motor. The inflow through the bearing groove, caused by the back pressure at the inner motor, cooled the heated space and moved upward. According to the thermo-flow analysis, the rotor inlet location should be shifted inward in the radial direction, and the rotor inlet and bearing groove geometries should be modified to achieve the optimal design.

When the rotor inlet location was at $X_1 = 114$ mm, the heat transfer rate was enhanced by 22% compared with the reference location. It was more important for cooling performance to have direct flow into the winding rather than an increased flow rate. A rotor inlet inner length of 12 mm increased the heat transfer rate by 3.7%. Of the various bearing groove geometries, only the threshold angle affected the cooling performance of the BLDC motor.

After a parametric study, three design parameters were selected for optimization: the rotor inlet, inner length, and threshold angle. An optimization using a response surface generated a model in which the performance was 24.3% better than the reference BLDC motor.

Acknowledgment

This study was supported by the research fund of Hanyang University (HY-2006-I).

References

[1] A.H. Bonnett, Operating temperature considerations and performance characteristics for IEEE 841 motors, IEEE Trans. Ind. Appl. 37 (2001) 1120–1131.
[2] S. Imao, M. Itoh, T. Harada, Turbulent characteristics of the flow in an axially rotating pipe, Int. J. Heat Fluid Flow 17 (1996) 444–451.
[3] T. Inamuro, A. Yamaguchi, F. Ogino, Fluid flow in a rotating cylindrical container with a rotating disk at the fluid surface, Fluid Dyn. Res. 21 (1997) 417–430.
[4] V. Sobolik, B. Izrar, F. Lusseyran, S. Skali, Interaction between the Ekman layer and the Couette–Taylor instability, Int. J. Heat Mass Transfer 43 (2000) 4381–4393.
[5] J.-Y. Hwang, K.-S. Yang, Numerical study of Taylor–Couette flow with an axial flow, Comput. Fluids 33 (2004) 97–118.
[6] M.-I. Char, Y.-H. Hsu, Numerical prediction of turbulent mixed convection in a concentric horizontal rotating annulus with low-*Re* two-equation models, Int. J. Heat Mass Transfer 41 (1998) 1633–1643.
[7] J.-S. Yoo, Mixed convection of air between two horizontal concentric cylinders with a cooled rotating outer cylinder, Int. J. Heat Mass Transfer 41 (1998) 293–302.
[8] Z.X. Yuan, N. Saniei, X.T. Yan, Turbulent heat transfer on the stationary disk in a rotor–stator system, Int. J. Heat Mass Transfer 46 (2003) 2207–2218.
[9] A.M. Raimundo, L.A. Oliveira, A.R. Figueiredo, Numerical simulation and experimental validation of heat transfer within rotating flows for three-dimensional non-axisymmetric, turbulent conditions, Int. J. Numer. Methods Fluids 40 (2002) 821–840.
[10] A.M. Raimundo, L.A.R. Figueiredo, A. Oliveira, Heat transfer measurements in a rotor–stator system with three-dimensional non-axisymmetric flow conditions, Exp. Therm. Fluid Sci. 27 (2002) 47–58.
[11] T. Nakahama, K. Suzuki, S. Hashidume, F. Ishibashi, M. Hirata, Cooling airflow in unidirectional ventilated open-type motor for electric vehicles, IEEE Trans. Energy Conver. 21 (2006) 645–651.
[12] S.V. Patankar, C.H. Liu, E.M. Sparrow, Fully developed flow and heat transfer in ducts having stream wise-periodic variations of cross-sectional area, ASME J. Heat Transfer 99 (1977) 180–186.
[13] M. Rokni, B. Sunden, A numerical investigation of turbulent forced convection in ducts with rectangular and trapezoidal cross-section area by using different turbulence models, Numer. Heat Transfer 30 (1996) 321–346.
[14] T.A. Harris, Rolling Bearing Analysis, Wiley, New York, 2001. pp. 461–578.
[15] B.E. Launder, N. Shima, Second-moment closure for the near-wall sublayer: development and application, AIAA J. 27 (1989) 1319–1325.
[16] T. Shih, W. Liou, A. Shabbir, Z. Yang, J. Zhu, A new k–ε eddy viscosity model for high Reynolds number turbulent flows, Comput. Fluids 24 (1995) 209–225.